



AFRL-AFOSR-UK-TR-2013-0044



On the Feasibility of multi-kHz Acquisition Rate Tomographic-PIV in Turbulent Flames

Isaac Boxx

**Deutsches Zentrum fur Luft- und Raumfahrt e.V.
Linder Hohe
Koln 511747
GERMANY**

EOARD Grant 12-2092

Report Date: October 2013

Final Report for 10 May 2012 to 09 May 2013

Distribution Statement A: Approved for public release distribution is unlimited.

**Air Force Research Laboratory
Air Force Office of Scientific Research
European Office of Aerospace Research and Development
Unit 4515 Box 14, APO AE 09421**

REPORT DOCUMENTATION PAGE

Form Approved OMB No. 0704-0188

Public reporting burden for this collection of information is estimated to average 1 hour per response, including the time for reviewing instructions, searching existing data sources, gathering and maintaining the data needed, and completing and reviewing the collection of information. Send comments regarding this burden estimate or any other aspect of this collection of information, including suggestions for reducing the burden, to Department of Defense, Washington Headquarters Services, Directorate for Information Operations and Reports (0704-0188), 1215 Jefferson Davis Highway, Suite 1204, Arlington, VA 22202-4302. Respondents should be aware that notwithstanding any other provision of law, no person shall be subject to any penalty for failing to comply with a collection of information if it does not display a currently valid OMB control number.

PLEASE DO NOT RETURN YOUR FORM TO THE ABOVE ADDRESS.

1. REPORT DATE (DD-MM-YYYY) 18 October 2013			2. REPORT TYPE Final Report	3. DATES COVERED (From – To) 10 May 2012 – 9 May 2013	
4. TITLE AND SUBTITLE On the Feasibility of multi-kHz Acquisition Rate Tomographic-PIV in Turbulent Flames			5a. CONTRACT NUMBER FA8655-12-1-2092		
			5b. GRANT NUMBER Grant 12-2092		
			5c. PROGRAM ELEMENT NUMBER 61102F		
6. AUTHOR(S) Isaac Boxx			5d. PROJECT NUMBER 5d. TASK NUMBER 5e. WORK UNIT NUMBER		
7. PERFORMING ORGANIZATION NAME(S) AND ADDRESS(ES) Deutsches Zentrum fur Luft- und Raumfahrt e.V. Linder Hohe Koln 511747 GERMANY			8. PERFORMING ORGANIZATION REPORT NUMBER N/A		
9. SPONSORING/MONITORING AGENCY NAME(S) AND ADDRESS(ES) EOARD Unit 4515 APO AE 09421-4515			10. SPONSOR/MONITOR'S ACRONYM(S) AFRL/AFOSR/IOE (EOARD)		
			11. SPONSOR/MONITOR'S REPORT NUMBER(S) AFRL-AFOSR-UK-TR-2013-0044		
12. DISTRIBUTION/AVAILABILITY STATEMENT Distribution A: Approved for public release; distribution is unlimited.					
13. SUPPLEMENTARY NOTES					
14. ABSTRACT <p>Tomographic particle image velocimetry (tomographic-PIV) is a recently developed measurement technique used to acquire volumetric velocity field data in liquid and gaseous flows. The technique relies on line-of-sight reconstruction of the rays between a 3D particle distribution and a multi-camera imaging system. In a turbulent flame, however, index-of-refraction changes resulting from local heat-release may inhibit reconstruction and thereby render the technique infeasible. The objective of this study was to test the efficacy of tomographic-PIV in a turbulent flame. An additional goal was to determine the feasibility of acquiring usable tomographic-PIV measurements in a turbulent flame at multi-kHz acquisition rates with current generation laser and camera technology. To this end, a setup consisting of four CMOS cameras and a dual-cavity Nd:YAG laser was implemented to test the technique in a lifted turbulent jet flame. While the cameras were capable of kHz-rate image acquisition, the laser operated at a pulse repetition rate of only 10 Hz. However, use of this laser allowed exploration of the required pulse energy and thus power for a kHz-rate system. The imaged region was 29 x 28 x 2.7mm in size. The tomographic reconstruction of the 3D particle distributions was accomplished using the multiplicative algebraic reconstruction technique. The results indicate that high quality tomographic-PIV measurements in a turbulent flame are possible with laser pulse energies of 25mJ, which is well within the capability of current-generation kHz-rate diode-pumped solid state lasers.</p>					
15. SUBJECT TERMS EOARD, Tomographic PIV, Turbulent Flames					
16. SECURITY CLASSIFICATION OF:			17. LIMITATION OF ABSTRACT SAR	18. NUMBER OF PAGES 27	19a. NAME OF RESPONSIBLE PERSON Gregg Abate
a. REPORT UNCLAS	b. ABSTRACT UNCLAS	c. THIS PAGE UNCLAS			19b. TELEPHONE NUMBER (Include area code) +44 (0)1895 616021

Final Technical Report

EOARD Grant: FA8655-12-1-2092

On the Feasibility of multi-kHz Acquisition Rate Tomographic-PIV in Turbulent Flames

Dr. I. Boxx
Institute of Combustion Technology
German Aerospace Center, Stuttgart

Abstract

Tomographic particle image velocimetry (tomographic-PIV) is a recently developed measurement technique used to acquire volumetric velocity field data in liquid and gaseous flows. The technique relies on line-of-sight reconstruction of the rays between a 3D particle distribution and a multi-camera imaging system. In a turbulent flame, however, index-of-refraction changes resulting from local heat-release may inhibit reconstruction and thereby render the technique infeasible. The objective of this study was to test the efficacy of tomographic-PIV in a turbulent flame. An additional goal was to determine the feasibility of acquiring usable tomographic-PIV measurements in a turbulent flame at multi-kHz acquisition rates with current generation laser and camera technology. To this end, a setup consisting of four CMOS cameras and a dual-cavity Nd:YAG laser was implemented to test the technique in a lifted turbulent jet flame. While the cameras were capable of kHz-rate image acquisition, the laser operated at a pulse repetition rate of only 10 Hz. However, use of this laser allowed exploration of the required pulse energy and thus power for a kHz-rate system. The imaged region was $29 \times 28 \times 2.7\text{mm}$ in size. The tomographic reconstruction of the 3D particle distributions was accomplished using the multiplicative algebraic reconstruction technique. The results indicate that high quality tomographic-PIV measurements in a turbulent flame are possible with laser pulse energies of 25mJ, which is well within the capability of current-generation kHz-rate diode-pumped solid state lasers.

Introduction

Fluid dynamic strain is a key driver of turbulent flame dynamics. It results from velocity gradients in the turbulent flow and therefore may occur in any direction. The full velocity gradient tensor has nine elements, corresponding to gradients in each of the three components of velocity along each of the three spatial axes. A key limitation in the study of turbulent flames is the inability of current measurement techniques to resolve all nine elements of the velocity gradient tensor simultaneously. The widely used particle image velocimetry (PIV) technique [Adrian, 1991] provides access to up to six elements of the tensor simultaneously in a plane but is unable to capture gradients perpendicular to the imaging plane. Researchers have attempted to address this limitation in various ways, usually via assumptions such as flow symmetry, global isotropy or the alignment of the flame orthogonal to the axis of in-plane principal compressive strain. Others have attempted to address the problem directly by acquiring multiple planes of PIV data simultaneously, or by acquiring data in single plane with sufficient temporal resolution to enable a 3D reconstruction of the flow that has passed through it. Pfadler et al. [2009, 2010] applied stereoscopic-PIV simultaneously in two parallel planes to measure the full nine-component strain-rate tensor in a premixed turbulent V-flame. This technique, while feasible in some flames, provides a relatively coarse, two-point approximation to the velocity gradient in the z-direction. As this method is based on linear interpolation of velocities measured in two separate, parallel laser sheets, it is also sensitive to misalignment of the laser sheets and to beam-steering resulting from index-of-refraction gradients through a flame. Ganapathisubramani et al., (2008) describes a technique wherein high frequency (kHz-framerate) stereoscopic-PIV is applied in a plane perpendicular to the axial flow direction of a gaseous jet, and Taylor's frozen flow hypothesis is used to reconstruct the quasi-instantaneous, 3D distribution of the velocity field that propagates through it. This technique has since been applied to study turbulence-flame interaction in premixed (Steinberg et al., 2009) and non-premixed (Gamba et al., 2013) turbulent flames. This technique, while robust and relatively straightforward to implement experimentally, is of limited utility in understanding the dynamics of turbulence-flame interaction, as it produces only quasi-instantaneous velocity field reconstructions.

Tomographic particle image velocimetry (tomographic-PIV) is a recently developed, three-dimensional measurement technique (Elsinga et al, 2006, Scarano, 2013), wherein multiple cameras are used to image tracer particles in a flow from several viewing angles simultaneously. With volumetric illumination and the use of objective lenses with sufficient depth of field (set by lens aperture, f-number setting) to keep the particles in focus throughout the illuminated region, it is possible to reconstruct the 3D distribution of tracer particles using optical tomography. The resulting particle distributions are then cross-correlated in a manner similar to conventional PIV to obtain 3D velocity fields. This technique has several clear advantages over conventional PIV, which measures velocity only in a plane. Chief among these is its ability to provide a direct measure of velocity gradients in all three dimensions, which is essential for accurate quantification of derivative quantities such as strain rates and vorticity. Application of this technique at kHz acquisition rates also yields highly resolved time-series measurements of these important turbulence quantities. As such, kHz-tomographic-PIV has the potential to revolutionize our understanding turbulence-chemistry interaction in turbulent-flames, where these quantities play a dominant role. Significant technical challenges, however, must be addressed if the potential of this measurement technique is to be realized.

The tomographic-PIV technique has only been fully characterized in non-reacting liquid and gaseous flows. Researchers have recently begun to attempt tomographic-PIV measurements in reacting flows (Lecordier et al., 2012, Coriton et al., 2013, Petersson et al., 2013) but to date there has been no rigorous or systematic study of the feasibility and limitations of this measurement technique in a turbulent flame. The aim of present work is to

thoroughly test the feasibility of accomplishing tomographic-PIV in a turbulent jet flame and to determine the feasibility of doing so at kHz acquisition-rates using commercially-available cameras and lasers.

Background

Technical challenges to kHz-rate tomographic-PIV in a turbulent flame

The primary technical challenges to accomplishing tomographic-PIV at multi-kHz acquisition rates in a turbulent flame are i) achieving sufficient illumination of the measurement volume and ii) reconstructing the particle scattering field in the presence of index-of-refraction changes (due to local heat-release of a flame). As will be shown below, both challenges appear surmountable through careful experiment design.

Achieving sufficient illumination for high quality tomographic-PIV in a turbulent flame seeded with micron-sized tracer particles is challenging but feasible with currently available laser and camera technology. Commercially available CMOS cameras (such as the Photron SA-X2) now achieve 12-bit dynamic range, 1024×1024 pixel imaging at 12,500 frames per second. Taking this as a reference for the current state of the art, it is feasible to estimate the achievable spatial resolution and illumination requirements for kHz acquisition-rate tomographic-PIV in a turbulent flame.

Assuming ideal, diffraction-limited optics, the depth of field (i.e. the region wherein all particles in the volumetrically illuminated measurement volume are in focus) of an imaging system may be computed according to the equation [Scarano, 2013]

$$\delta z = 4.88 \lambda f_{\#}^2 \left(1 + \frac{1}{M}\right)^2$$

where δz is the depth of focus, λ is the laser wavelength, $f_{\#}$ is the f-number of the imaging objective and M is the system magnification. The lifted turbulent jet-flame studied in this work has a full-width diameter of approximately 28mm at the mean lift-off height. Based on the 20 micron pixel size of a current generation kHz-rate CMOS camera, a magnification factor of approximately 0.7 would be required to capture this dimension. Assuming illumination at $\lambda = 532\text{nm}$ (i.e. with a frequency-doubled Nd:YAG laser) and ideal, diffraction-limited optics a depth of field of approximately 2.7mm would be achieved with an f/16 imaging objective.

The need for volumetric illumination and a small aperture (high f-number) necessitates the use of a laser with significant pulse energy. Based on prior experience with conventional, planar stereoscopic-PIV [Boxx et al., 2010] excellent quality PIV may be accomplished in an enclosed, swirl-stabilized turbulent flame seeded with 1-micron diameter titanium dioxide particles with a laser fluence of 0.1mJ/mm^2 . Indeed, excellent vector yield was achieved throughout the entire field of view. Imaging in the study of Boxx et al. (2010) was performed with 100mm focal length objective lenses with apertures set to f/5.6. Based on a simple geometric calculation, the volumetric illumination of a region 30 mm tall and 3 mm deep thus requires a 7.6 mJ laser pulse. Multiplying this requirement by eight to account for the difference in f-stop setting (f/16 rather than f/5.6), one arrives at a required pulse-energy of approximately 60mJ. This is significantly beyond the state of the art of current generation frequency-doubled DPSS lasers in the 5-10 kHz range. A brief market survey by the authors indicates the highest pulse-energy achievable with current generation, ‘off the shelf’ lasers in this range is approximately 15-20mJ / pulse. However, the fluence used for the scaling calculation does not represent a detection limit, only a value from a previous experiment that produced high PIV vector yield. Furthermore, the current generation of CMOS cameras (e.g., the Photron SA-X2 and the Phantom v1210 and v1610 cameras) has significantly improved detection limits over that used in Boxx et al. [2010]. Finally, it may be feasible to retro-reflect

the probe beam through the medium, thereby effectively doubling the energy delivered. It should be noted too that retro-reflection of the beam improves the uniformity of the scattering signal between the cameras, as each will see both forward- and back-scattered laser radiation.

The second technical challenge to successfully accomplishing tomographic-PIV in a turbulent combustion environment is reconstruction of the particle scattering field in the presence of index-of-refraction changes (associated with local density variation induced by heat-release of the flame). The tomographic reconstruction technique requires that linear (line-of-sight) rays between particles in the measurement volume and their projected 2D images on the camera arrays intersect at a discrete point in space. Successful triangulation of the particle location therefore requires that these rays intersect to within a fraction of the diameter of the projected particle image. Successful reconstruction of particle distributions depends on a spatial calibration accurate to within 0.4 pixels (Elsinga, et al. 2006). Through careful calibration using a physical imaging target and subsequent application of a self-calibration routine based on cross-correlation of particles in quiescent environment it is relatively straightforward to achieve a calibration accuracy of 0.1 pixels or better.

However, distortion of the line-of-sight projection of particle images onto the imaging array has the potential to affect the accuracy of the geometric calibration. This effect has been studied for the case of 2- and 3-component planar PIV in flames by Muniz et al. (1996) and Han, et al. (2000), respectively. Muniz et al. (1996) determined the effect “flame-induced” distortion to be negligible for two-component PIV, whereas Han et al., (2000) observed distortions ranging from 0.2 to 0.9 pixels in rays projected through a hydrogen jet-flame vs. those projected through a cold flow. The measured distortion however, scales with a number of factors, including imaging system magnification (and pixel size), distance of the cameras from the imaging plane and the number of hot-cold gas interfaces traversed by the projected rays. Each of these parameters is significantly greater in the Han, et al. (2000) study than in the present work, but of course each experimental setup will produce different levels of flame distortion. Furthermore, as the diffraction-limited blur-spot size for this imaging configuration is approximately 31 microns, equaling only 1.5 pixels (highlighting the beneficial effect of large pixels), flame distortion leading to image blur that is less than say 20 microns will be of little consequence.

Experiment Configuration

In order to test the feasibility of accomplishing tomographic-PIV at kHz acquisition rates in a turbulent flame using only current-generation, commercially available technology we implemented a tomographic-PIV system subject to the illumination and imaging configuration constraints described above. The system was then used to study the stabilization region of a turbulent lifted jet-flame of methane in a low velocity co-flow.

The experimental setup is shown schematically in Figure 1. The tomographic PIV system consists of two components, the four-camera imaging system and the volumetric illumination system. These are described separately in the section below. The system was operated at 10Hz. The lifted jet flame burner and run conditions are described separately.

Illumination

The measurement volume was illuminated at 532nm by a dual-cavity, flashlamp-pumped Nd:YAG laser (New Wave Solo-PIV). Timing separation between laser pulses was set to 10 or 20 μ s, depending on imaging location. The maximum power of this laser is 120mJ per pulse. In the present study, neutral density filters were used to attenuate the pulse energy to either 25 or 40mJ per pulse, depending on the experiment run conditions. This beam attenuation was designed to duplicate the maximum pulse energy available from current-generation diode-pumped solid state (DPSS) lasers with multi-kHz repetition rates. The volumetric illumination optics consisted of a spherical telescope, followed by a cylindrical

telescope. The spherical telescope consisted of a pair of spherical lens; the first with a focal length of -82mm and the second with +150mm, to approximately double the initial beam diameter. The cylindrical telescope was used to expand the beam vertically and collimate it. The telescope used a pair of cylindrical lenses, the first of which had a focal length of -38mm and the second +250mm. The resulting beam was approximately 27mm tall. A set of knife-edges were used to block the low-intensity wings of the beam and thus prevent stray light from affecting the measurement. The knife edges were mounted 3mm apart, to limit the beam thickness to that width. A retro-reflecting mirror was used to pass the beam through the illuminated region a second time, and apertures placed in the beam path provide an easy means of aligning the retro-reflector.

Imaging System

Particle images were recorded on four CMOS cameras mounted in a linear array aligned on one side of the measurement volume. The outer two cameras of this array subtended an angle of 88 degrees, and the inner pair 28 degrees. Each camera had a 1024×1024 pixel imaging array and was equipped with a 200mm, f/16 imaging objective (Nikon, AF-Nikkor). Each camera was coupled to its objective using a Scheimpflug adaptor, in order to correct for blurring caused by off-axis imaging. The Scheimpflug adaptors were aligned such that the focus plane of each camera was aligned to the center of the measurement volume. Two of the cameras (both LaVision HSS5) had 10 bit ADC dynamic range imaging arrays capable of full-frame acquisition rates of up to 3000 fps. The two remaining cameras (a LaVision HSS6 and HSS8) had 12 bit ADC dynamic range imaging arrays capable of full-frame imaging at 5000 and 7500 fps, respectively. These cameras were used both because they were available at our laboratory and because their CMOS imaging arrays have sizes and pixel dimensions similar to the current state-of-the-art in this field. The dimensions of the measurement volume were $29 \times 28 \times 2.7$ mm. Images were acquired at three imaging locations, including one at the jet-centerline beginning 8mm downstream of the jet-exit and two in the vicinity of the flame leading edge, beginning approximately 42 mm downstream of the jet-exit.

The cameras were operated in full-frame imaging mode, synchronized to the laser via a digital delay generator (Quantum Composers 9528) and a timing synchronization / control module (LaVision Highspeed Controller). The minimum stable acquisition rate of the cameras was 60Hz. The cameras were therefore operated in full-frame imaging mode at that frequency, resulting in a dual-frame imaging rate of 30 Hz and single-frame exposure times of 16.7ms. The 10 Hz repetition rate of the laser resulted in every third dual-frame image of the sequence being illuminated. The onboard memory of the cameras enabled the acquisition of 1024 image pairs per imaging run. As only one third of these images were illuminated, 341 dual-frame tomographic-PIV measurements were acquired per imaging run.

Jet-flame Burner

The axisymmetric jet flame burner consists of an 8mm inner diameter fuel tube, which supplies a jet of methane with 16.5m/s mean velocity at the exit. The fuel tube is tapered from 10mm outer diameter to a sharp edge at the jet-exit. The fuel jet is surrounded by a concentric nozzle of 140mm diameter. This nozzle is preceded by a settling chamber and a series of perforated plate flow-conditioning elements. It supplies a low-speed (310 g/min, or 0.27 m/s mean velocity) co-flow of air to ensure stable and reproducible boundary conditions at the lifted flame base. Both the jet and the co-flow were seeded with titanium dioxide particles with a nominal mean diameter of 1 μ m. Flow rates of the fuel and co-flow air were monitored throughout the experiment via calibration-standard Coriolis mass flowmeters (Siemens Sitrans-FC Mass-Flo 2100, Model DI-3 and DI-15 respectively).

Data Processing

Image pre-processing

A series of pre-processing steps was applied to the particle images prior to tomographic reconstruction of the 3D particle distributions. The effect of each pre-processing step is illustrated in Figure 2. First, a 3×3 pixel sliding minimum subtraction was applied, to remove the diffuse flame luminosity. Next, the images were normalized to the 100×100 pixel local average, to reduce the effect of illumination nonuniformity. The intensity distributions of all four cameras were then normalized to a single value. To improve contrast in the low seed-particle density regions around the flame, a Gaussian filter (window size 3×3 pixel), followed by a sharpening filter was applied. To further improve contrast and reduce the effect of fixed-pattern noise from the camera, a constant intensity (10 counts) was subtracted from each pixel. Finally, the pre-processed image was multiplied by a constant, to reduce the effect of rounding error when the particle images are stored in integer format prior to tomographic reconstruction.

Volumetric Calibration

Volumetric calibration was accomplished by acquiring a series of five images of a dual-plane imaging target (LaVision Type 7) that was traversed through the measurement volume of the PIV system on a micrometer-actuated translation stage. Each target image consisted of an ensemble-average of 100 frames acquired from the corresponding camera, in order to eliminate background noise from the CMOS imaging arrays. Displacement of the target from image to image was 1mm in the z- (through-plane) direction. The Type 7 dual-plane calibration target has circular reference dots separated by 5mm on each plane, and a planar separation of 1mm. The calibration images therefore contained between 25 and 36 calibration points on each plane, depending upon z-location. Based on these images, a volumetric calibration was performed using a pinhole camera model implemented in a commercial PIV analysis package (LaVision Davis 8.1). The accuracy of the initial mapping function was between 0.4 and 1.2 pixels, depending on the camera. This mapping function was then refined using volumetric self-calibration (Weineke, 2008) to achieve a mapping function accurate to within 0.02 pixels. A new multi-plane calibration and self-calibration procedure was performed each day.

Volumetric Reconstruction and Cross-correlation

Reconstruction of the 3D particle distributions was accomplished using the multiplicative algebraic reconstruction technique (MART – Elsinga et al., 2006), with 10 iterations. The resolution of the particle image reconstructions is 37.7 voxels / mm. The reconstructed volume measures $29 \times 28.2 \times 6$ mm, or $1096 \times 1062 \times 226$ voxels. Although the depth of the reconstructed volume is larger than the illuminated region (6mm vs 3mm), the additional reconstruction volume is a useful check on the quality of the tomographic reconstruction, as any particles reconstructed beyond the illuminated volume are clearly non-physical, or “ghost-particles”. This effect will be discussed in greater detail in a later section of the paper.

Velocity field data was extracted from the reconstructed 3D particle distributions via an adaptive window offset, 3D particle cross-correlation algorithm. The initial window size for this correlation was $128 \times 128 \times 128$ voxels, and the final one was $64 \times 64 \times 64$, with 75% vector overlap. This corresponds to a vector resolution of approximately 1.7mm cubed, and vector spacing of 0.43mm. Spurious vectors were detected and removed via the universal outlier detection method proposed by Westerweel and Scarano (2005), and replaced with

vectors corresponding to the average of the surrounding $3 \times 3 \times 3$ vectors. The resulting 3D velocity field data was then smoothed with a single-pass, $3 \times 3 \times 3$ Gaussian filter.

Results

The primary goal of the present study was to investigate the feasibility of performing tomographic-PIV in a turbulent, reacting flow and to judge the feasibility of doing so at kHz frame-rates using currently available laser and camera technology. The results and discussion presented below therefore focus primarily on those parameters relevant to judging the potential (and the limitations) of this measurement technique in reacting flows. The secondary goal, however, was to investigate the 3D flowfield associated with a canonical lifted jet flame.

Vector Validation

A quantity of interest in judging the quality of PIV measurements is the percentage of vectors removed and replaced during vector validation. Figure 3 shows profiles representing the percentage of vectors removed during vector validation (integrated over the entire x-y plane and over a full 341 frame acquisition run) vs. z-direction. Figures 3a and 3b show the profiles for the downstream measurement locations. Figure 3c shows the percentage of removed/interpolated vectors at the jet-exit measurement location. The $z = 0\text{mm}$ plane in these plots corresponds to the jet-centerline. Several important characteristics are apparent in these profiles.

At the jet-exit measurement location (where there is no flame), the profile is reasonably uniform across the measurement volume, with a decrease in valid vectors toward the lower-intensity wings of the illuminated volume. In the uniform region, 1-2% of all vectors were removed during vector validation. This small percentage compares well with conventional stereo-PIV measurements and is a good vector yield in any case. The profiles measured at the downstream locations show considerably less uniformity and a larger percentage of removed/interpolated vectors. In Figure 3a, which corresponds to the downstream measuring location illuminated with 40mJ/pulse, we observe between 2.5 and 8% of vectors are removed through vector validation. In Figure 3c, corresponding to 25mJ illumination, between 3 and 9% of vectors are removed / replaced.

Comparison of the profiles for the reacting- and non-reacting flows in Figures 3a and 3b indicates that, on average, the presence of a flame does not significantly influence the vector yield for this measurement. At 40mJ illumination, the profiles overlap both in shape and magnitude. For the case of 25mJ illumination, the reacting flow measurement actually shows a higher vector yield than the non-reacting condition at the same location. Taken together, it is reasonable to conclude that the presence of a flame does not significantly affect the mean tomographic-PIV vector yields for the imaging configuration and conditions studied in the present work.

Ghost Particles and SNR

A key measure of the quality of a tomographic particle reconstruction is the ratio of real-particles in a reconstructed volume to non-physical artifacts known as “ghost particles”. Ghost particles in a tomographic PIV reconstruction occur as a result of the line-of-sight reconstruction between particles and the cameras (Maas et al., 1993). It has been shown (Elsinga et al., 2006) that as the seed-particle density in a flow is increased the number of non-physical “ghost particles” in a tomographic reconstruction also increases. Ghost particles are effectively noise in the particle reconstruction and they decrease the contrast of the volumetric cross-correlation used to determine velocity fields. The percentage of non-physical or “ghost” particles in a measurement may be determined by comparing the mean integrated signal of the 3D particle reconstruction within and beyond the illuminated volume according to the relation,

$$\% \text{ Ghost Particles} = (I_{ov}) / (I_{iv} - I_{ov}) \quad (1)$$

where I_{ov} is the integrated signal outside the illuminate volume, and I_{iv} is the integrated signal level within the illuminated volume. The reciprocal of this number may be interpreted as the signal-to-noise ratio (SNR) of the particle reconstruction.

Figure 4 shows the profiles of the integrated signal intensity vs. z-direction for each laser at the jet-exit measurement location. These profiles are integrated over the entire xy-imaging plane and averaged over a single imaging run of 341 measurements. The mean integrated signal level outside the illuminated region (for both profiles) was 0.08 a.u. (arbitrary units). The mean integrated signal level for Lasers 1 and 2 were up to 0.73 and 0.64, respectively. Applying Eq. 1, we see the percentage of ghost particles in the reconstructed particle distributions was approximately 12 - 14% for this measurement location, corresponding to a SNR of 7 - 8 at this location. This is well above the cutoff value (SNR > 2; Scarano, 2013) required for good-quality tomographic-PIV. Figures 5 and 6 show integrated signal profiles for the downstream measurement locations. Figure 5 shows the profile for the non-reacting jet (left) and lifted jet-flame (right) for the 40mJ illumination measurement. Applying Eqn. 1, it can be shown that the SNR for this case is even higher than at the jet exit, ranging up to 19 - 26 for the non-reacting jet and 11 - 14 in the lifted jet flame. As expected, the SNR for the 25mJ illumination condition (shown in Figure 6) is significantly lower, from 9 - 10 for the non-reacting jet to 11 - 12 in the lifted jet flame.

Although the SNR for the downstream measurement locations is comparable to, or higher than at the jet-exit, Figure 3 indicates a significant difference in the vector yield between the measurement locations. The reason for this difference in first-choice vector yield is not immediately clear. Figures 4 - 6 indicate differences in SNR of the particle reconstructions are not the cause. The similarity in vector yield profiles for the reacting and non-reacting flows downstream indicates the difference does not result from the presence of a flame in the measurement volume. Comparing the profiles of mean integrated signal for each measurement location with the profiles of validated vectors suggests the difference results from poor beam-overlap at the low-intensity wings of the laser-illuminated measurement volume. For example, in Figure 3c (at the jet-exit location) the vector yield drops off sharply between $z = 3$ and 3.5mm. Comparing this to the same location in Figure 4, we see a significant misalignment of the integrated signal profiles that results in much lower illumination from Beam 1 relative to Beam 2. Similarly in Figure 3b, a rapid drop in vector yield occurs between $z = 2.5$ and 3mm and one sees a similar change in mean integrated signal intensity over the same region in Figure 6. Based on these observations, it is reasonable to conclude that accurate beam-overlap, particularly at the low-intensity wings of the measurement volume, has a more significant limiting effect in this case than the presence of a flame.

Seed Particle Density

As with conventional (planar) PIV, the spatial resolution achievable with tomographic-PIV is strongly linked to the concentration of seed particles in the flow. It has been shown that for a robust cross-correlation, an interrogation volume should contain at least 5-10 particles (Scarano, 2013). It is well-established however, that the percentage of ghost particles in a tomographic reconstruction increases with increasing seed particle concentration (Elsinga et al., 2006). Elsinga et al. (2006) have shown that for a four camera tomographic imaging system, the optimal seed particle concentration (i.e. the highest concentration that still produces a tomographic reconstruction of acceptable quality) is approximately 0.05 particles per pixel (ppp).

Seed particle concentrations in this study were determined by applying an intensity threshold to binarize the (pre-preprocessed) seed-particle images and counting the number of particles in the frame. As each camera had a different viewing angle and, therefore, a slightly different field of view, concentrations were estimated from the images of only one of the four cameras. The mean particle concentrations are listed in Table 1 (below).

Table 1 – Seed particle concentration

Run Condition	Particles (total)	ppp	Concentration (mm ⁻³)	Particles per 64 voxel IB	Particles per 32 voxel IB
40mJ illumination, At jet-exit	34397	0,033	14.5	71	9
40mJ Non-reacting jet	26824	0,026	11.4	56	7
40mJ Lifted jet flame	35008	0,033	14.9	73	9
25mJ Non-reacting jet	18872	0,018	8	39	5
25mJ Lifted jet flame	32548	0,031	13.8	67	8

The seed particle concentrations were estimated with the assumption that the seed particles were evenly distributed through the entire 28 × 28 × 3mm illuminated volume. With the same assumption, the average number of particles in a 64³ and a 32³ voxel interrogation box were estimated.

The values in Table 1 are best-estimate values based on particles counted in a single frame of the four-camera system. Nonetheless, they provide a useful base for comparison between both prior studies and between individual run conditions in the present study. It is clear from Table 1 that the seed particle density in the present study was significantly below the optimal level of 0.05ppp observed by Elsinga et al. (2006). The estimated seed particle concentration (particles / mm⁻³) in the present study however, is significantly higher than that typically reported for studies of non-reacting gaseous flows (Scarano, 2013). Although seed particle concentrations are not typically reported in studies applying conventional PIV, concentrations much greater than 0.05ppp are typically used to study turbulent flames in order to ensure sufficient seed particle concentration for robust cross-correlations in regions of both burned and unburned gas. Indeed, the drop in seed particle density is so clear that it is frequently used as to identify the reaction zone in PIV studies of premixed turbulent flames (Pfadler et al., 2007). The relatively high seed-particle concentration in the present study was intended to help ensure adequate seed concentration in low-density regions created by heat-release of the flame.

Based on the estimate of 5-10 particles per interrogation box being required for robust cross-correlation, Table 1 provides an estimate of the achievable vector resolution in this study. In the present study, a 64³ voxel interrogation box contains, on average, ca. 40 – 70 particles. This is clearly above the threshold required to achieve robust correlations. Assuming fluid reaches the adiabatic flame temperature of methane (ca. 2200K), the seed particle density will drop by a factor of approximately 7.5. Therefore, interrogation boxes in regions of burned gas may be expected to contain 5-9 particles, which is at or above the threshold required for robust correlations. For comparison, Table 1 indicates a 32³ voxel interrogation box contains (on average) 5-9 particles in regions of unburned gas and < 2 particles in regions of burned gas. Therefore, while a 32³ voxel interrogation box may yield viable vectors in regions of unburned gas, it is clearly unsuitable for the reacting flow condition; indeed, particle densities of 3 to 4 times that used would be needed for robust

correlations. As will be shown in the following section, a visual inspection of the vector fields readily confirms this conclusion.

Comparing the seed particle concentrations for each run condition in Table 1 yields one more insight into the results of the present study. Returning to the profiles of vector yield discussed earlier, Figure 3 shows a measurably greater vector yield in the reacting jet data than in the non-reacting jet with illumination of 25mJ. All things being equal, this result is counter-intuitive, considering the density gradients and background luminosity present in the reacting jet. Table 1 shows that the seed particle density in the non-reacting jet measurement was significantly lower than in the reacting jet. This, combined with the poorer laser sheet overlap discussed previously, provides a reasonable explanation for the decreased vector yield.

Vector Resolution vs. Correlation Noise

In order to determine the sensitivity of our measurement to interrogation volume size, several measurements were processed at multiple interrogation volume sizes. One such measurement is shown in Figure 7. The velocity field data in this figure is derived from the particle field images shown Figure 2. In this figure, a single measurement frame was processed at $64 \times 64 \times 64$, $48 \times 48 \times 48$, $32 \times 32 \times 32$ and finally $24 \times 24 \times 24$ voxels, each with 75% vector overlap and identical post-processing steps. For clarity, only every second vector is displayed. Also shown are isosurfaces representing -2500s^{-1} (blue) and $+2500\text{s}^{-1}$ (red) vorticity.

Comparing the four frames of Figure 7, it is clear the velocity field measurement becomes significantly noisier as the size of the interrogation volume is reduced. Comparing the first two frames, which correspond to 64^3 and 48^3 voxels, respectively, one sees clear similarity in the large-scale structure of the vorticity isosurfaces. The isosurfaces in the 48^3 voxel correlation show more fine-scale texture compared to those of the 64^3 voxel correlation. This results from both the higher measurement resolution and the increased noise resulting from the smaller interrogation volume. The isosurfaces, however, remain clearly recognizable from one resolution to the next. Comparing the isosurfaces in the second and third frames of Figure 7, one sees a dramatic increase in fine-scale structure. A comparison of the large-scale structure of the vorticity isosurfaces in Frames a and b with that in frame c shows some similarity but this is masked by the extensive fine-scale structure present throughout most of the measurement volume. The large extent and quasi-random distribution of this fine-scale structure strongly suggests it results from numerical noise rather than from physical vorticity. In Frame d, which corresponds to 24^3 voxel interrogation volumes, numerical noise is clearly dominant. Although some similarity between the 64^3 and the 24^3 voxel results can be seen, it is unlikely that the velocity measurements obtained through a cross-correlation based on 24^3 voxel interrogation volume would be usable.

Based on this resolution vs. noise test, the vectors in this study were processed using 64^3 voxel interrogation volumes which, at 38 voxels/mm, corresponds to an interrogation volume size of 1.7 mm cubed. This resolution is comparable to that typically obtained with the tomographic PIV technique in non-reacting gaseous flows (Scarano, 2013). Although it is perhaps unsurprising to note the spatial resolution and SNR attained in the present work are comparable to those in prior studies that use the same technique, it is important to bear in mind that these were attained despite imaging through the flame. Given the quality of the vector fields shown in Figure 7, it is reasonable to conclude that flame-based image distortion is not significant for the flow-conditions studied in this work.

Single-Shot Measurements

As an additional check of the vector quality, single-frame measurements were inspected 'by eye'. The goal of these checks was judge the quality of the vector fields based on physical

considerations and prior experience with conventional planar PIV measurements. Figure 8 shows a typical, single-shot measurement acquired with 40mJ illumination in the non-reacting jet (left) and the lifted jet-flame (right). These measurements were processed with 64^3 voxel interrogation volumes and the parameters described earlier. The isosurfaces represent -2500s^{-1} (blue) and $+2500\text{s}^{-1}$ (red) vorticity. The measurement on the right side is from the same measurement shown in Figure 7. Several important features are evident in this figure.

First, comparing the spatial dimensions and structural features (curvature, axial and radial distribution, etc.) of the vorticity isosurfaces in the reacting and non-reacting flows, one sees the two are quite similar. This is consistent with what we know of lifted turbulent jet flames, i.e. that the effect of the flame is limited largely to the periphery of the jet where the flamefront resides. The similarity of the vorticity isosurfaces for the two cases suggests the presence of a flame in the measurement volume does not strongly affect the velocity measurement. In addition, we see little variation in the structure and distribution of the vorticity contours upstream or downstream of the flame location (seen in Figure 2), further supporting the conclusion that flame has a limited effect on the measured velocity field data.

Figure 9 presents profiles of axial-, radial- and azimuthal- (through-plane) velocity from the measurements in Figure 8. The profiles are taken 60mm downstream of the jet-exit, at six different z-locations. The purpose of these profiles is to judge the plausibility of the vector data. For example, in the profile of axial velocity in the non-reacting jet measurement (left), one observes a local peak in the $z = 0\text{mm}$ profile at approximately $r = 6\text{mm}$. Similar peaks appear in each of the neighboring z planes shown in this figure, as one would expect in the case of a turbulent flow structure. The profile of radial velocity shows a local peak at the same location, albeit without significant variation in the z-direction. Finally, a strong variation in the azimuthal velocity profiles is observable at this radial location. The smooth variation of this profile feature with z-direction, combined with the fact that it appears in the profiles of all three components of velocity indicates this feature is a physically plausible representation of a turbulent flow structure. In contrast, observe the velocity profile for $z = -2.12\text{mm}$ in the reacting flow case. At approximately $r = 15\text{mm}$ one observes a profile feature that is likely non-physical. The profile feature indicates a sudden flow reversal and jump in radial and azimuthal velocity. This profile feature appears near the edge of the illuminated measurement volume and does not appear in the profiles for neighboring azimuthal-planes. Examination of the corresponding spatial coordinates ($x = 15\text{mm}$, $y = 60\text{mm}$, $z = -2.12\text{mm}$) in Figure 8 reveals a small-scale feature in the vorticity isosurfaces. The small size and isolated location of this structure, suggests it is a measurement artifact (such as a cluster of spurious vectors not eliminated by the vector validation routines), rather than a small counter-rotating vortex pair, as it may appear upon first inspection.

Figure 10 shows a typical, single-frame measurement acquired with 25mJ illumination in the non-reacting jet (left) and the lifted jet-flame (right). Figure 11 shows the corresponding profiles of axial, radial and azimuthal velocity 60mm downstream of the jet exit. Similar characteristics to those identified in the 40mJ measurement are identifiable in these figures. In both the non-reacting and the reacting flow measurements, the structure and distribution of the vorticity isosurfaces are quite similar. Key features in the velocity profiles shown in Figure 11 show continuous variation from one z-location to the next and consistency between axial-, radial- and azimuthal velocity fluctuations. The profiles in Figure 11 are coarser than those in Figure 8, reflecting the decreased SNR resulting from the weaker illumination, but otherwise are plausible from a physical standpoint.

Vector Statistics

Jet-Exit Imaging Location

Figure 12 shows the mean, 3D velocity field of the lifted jet-flame, measured with 40mJ/pulse (and laser retro-reflection). Although this figure shows data measured in the flow-field of a lifted jet-flame, the flame-base remained downstream of the measurement volume throughout this imaging run. As the flame is not expected to significantly affect the flow upstream, no corresponding measurement of the non-reacting jet was made at this location. The isosurfaces shown correspond to mean axial velocities of 2 m/s (blue), 10 m/s (green) and 21m/s (orange), respectively.

The smoothness of these isosurfaces suggests the data are well-converged in the mean at this location. Figure 13 shows the profiles of mean and fluctuating axial velocity in the plane corresponding to the jet-centerline at the most upstream location (8mm from the jet-exit) of Figure 12. Based on the L/d of the tube from which the jet issues, the velocity profile at the jet-exit is expected to be that of a fully developed turbulent pipe flow. Although the axial velocity profile was not measured directly at the jet-exit, the profile shown in this figure is consistent with the prediction of fully developed turbulent pipe flow. Figure 14 shows the profiles of mean (left) and fluctuating (root mean square, RMS) axial velocity at the centerline for increasing downstream distance from the jet-exit. As expected, the mean velocity profile shows a transition from fully developed turbulent pipe flow in the near field to the familiar, Gaussian-shaped profile of a free jet with increasing downstream distance. The growth of the shear-layer at the periphery of the jet is clearly identifiable in the profile of RMS axial velocity. Taken together, these figures show the velocity field data is well-converged in the near-field imaging location.

Downstream Imaging Location

Figure 15 shows the mean, 3D velocity fields measured in the non-reacting jet (left) and the lifted jet flame (right) at the downstream imaging location with 40mJ/pulse illumination and retro-reflection. Figure 16 shows the corresponding plot for the case with 25mJ/pulse illumination (and retro-reflection). The isosurfaces represent mean axial velocity and correspond to 3m/s (blue), 10m/s (green) and 15m/s (orange). Comparing the isosurfaces of axial velocity in Figure 15, it is clear that the lifted jet flame does not strongly affect the mean velocity profile at this location. The velocity field for the lifted jet flame shows a slightly greater radial spread in the low-velocity periphery compared to that of the non-reacting jet, an effect which likely results from dilatation caused by heat-release in the flame. The higher-velocity isosurfaces are virtually identical in profile. Similar features are also apparent in the 25mJ/pulse measurement.

Figure 17 shows profiles of axial velocity along the jet centerline for increasing downstream distance from the jet-exit in the 40mJ illumination measurement. The Gaussian-shaped velocity profile of a turbulent free-jet is readily apparent in these profiles, indicating the data is well-converged in the mean. The peak centerline velocity decay and growth in jet diameter with downstream distance are also well-captured in both the non-reacting jet and jet-flame measurements. The profiles confirm the earlier observation that the jet spreads slightly quicker when a lifted jet flame is present than when it is not.

Figure 18 shows profiles of axial velocity fluctuation at the same downstream distances as the profiles of Figure 17. It is well known that higher order statistics converge significantly less quickly than those of the mean, and, as expected, the profiles in Figure 18 are noticeably less converged than those in Figure 17. The trends observable in both the non-reacting jet and the jet-flame data are consistent with what one would expect for a free turbulent jet: i.e., peak fluctuation intensity in the shear-layer that decreases in magnitude and broadens radially with increasing downstream distance. A comparison of the profiles for the non-reacting jet and the jet-flame shows the two are surprisingly similar. The peak fluctuation intensity is virtually identical for both cases, as is the radial growth rate. Consistent with the trend observed in the mean velocity profiles, the profiles of fluctuation intensity show greater radial growth with

downstream distance than those of the non-reacting jet. The magnitude of the fluctuating components, however, is remarkably similar. This suggests both that the flame does not strongly influence the velocity field at mean flame-base location and that it does not significantly affect the accuracy of the tomographic-PIV measurement there.

Figure 19 shows profiles of mean axial velocity at increasing downstream locations for the measurement with 25mJ illumination. As expected, these profiles also show the Gaussian shape of a turbulent free jet, albeit with noticeably greater distortion than those in Figure 17. For example, one observes a dip in mean axial velocity to the left of the jet centerline in the profiles for the non-reacting jet at 56 and 60mm downstream. Deviation from the Gaussian-shape mean velocity profile, particularly in high-velocity centerline region of the jet seems to indicate that the velocity field statistics are not as well converged there.

Figure 20 shows the profiles of axial velocity fluctuation (RMS) for the corresponding downstream distances. Several features observable in this figure confirm the observation that the data are not as well converged in this measurement series as with 40mJ illumination. For example, the profiles for 51mm, 56mm and 60mm downstream in the non-reacting jet show significant (left / right) asymmetry in peak fluctuation magnitude. In addition, the peak fluctuation intensity for the 45mm downstream location appears near the jet-centerline, a clearly non-physical result, given the known flow-field characteristics. Similar, albeit less severe asymmetry is observed in the lifted jet flame profiles.

Despite poorer convergence in the regions of peak fluctuation intensity, the profiles of axial velocity fluctuation measured with 25mJ illumination are consistent with those measured with 40mJ. Figure 21 shows the fluctuation intensity profiles for each measurement, 60mm downstream the jet-exit and overlaid on a single axis. Outside the region of peak fluctuation intensity (i.e. the shear-layer region), the profiles overlap well. The profile measured with 25mJ illumination shows slightly higher fluctuation intensity than that measured with 40mJ, particularly in the highest-magnitude portions of the curve, but has a similar value on the jet centerline. The fact that both the reacting and the non-reacting measurements show similar reproducibility, with deviations of similar magnitude in the regions of high velocity fluctuation indicates the presence of a flame in the measurement volume does not significantly affect the overall accuracy of the measurement.

Discussion

Tomographic PIV is a well-developed measurement technique and has been extensively characterized and successfully applied in a range of liquid-, and non-reacting gaseous flows. With its ability to visualize and track the spatiotemporal evolution of complex turbulent flow structures, this technique has the potential to revolutionize our understanding of turbulence-flame interactions. Before this potential can be realized however, it is important to understand both the strengths and the potential limitations of this technique.

The results presented above demonstrate several important points to consider when applying tomographic PIV in a turbulent flame. The first of these is that it is indeed possible to acquire three-dimensional velocity field data in a turbulent flame. Furthermore, it is possible to do so at kHz acquisition rates using only current generation laser and camera technology. It is clear from the results presented above that index-of-refraction changes at the flame front do not prevent the tomographic reconstruction of the 3D particle distribution in the flow studied here. Furthermore, the results indicate that index-of-refraction changes induced by heat-release at the flame do not prevent the effective use of a retro-reflecting mirror to increase the illumination intensity of the laser. It is not clear from this study if a multi-pass cell of the type described by Ghaemi and Scarano (2010) would be viable for imaging a turbulent flame, but a single-pass retro-reflecting mirror is both a viable and effective means by which to increase the illumination of the measurement volume and

equalize scattering signals for the cameras (as each views both back and forward scattered radiation).

The primary limitation of tomographic-PIV as an effective tool for investigation of turbulence-flame interactions appears to be one of volumetric resolution. A reliable line-of-sight reconstruction of 3D particle distributions requires a significantly lower seed density than is typically achievable with stereo-PIV. As the minimum achievable spatial resolution is coupled to the number density of seed particles in the flow, this limits the volumetric resolution achievable with tomographic-PIV. The drop in seed particle density that accompanies volumetric expansion caused by the flame exacerbates this problem. In the present study, a volumetric resolution of approximately 1.3 - 1.7mm was achieved, which is comparable to most tomographic-PIV studies reported in the literature (Scarano, 2013). Although overlap of the interrogation volumes enables a much smaller vector spacing than the (1.3-1.7mm) vector resolution, this resolution constitutes a significant fraction of the 8mm jet-exit diameter and approximately 10mm (FWHM) jet width at the flame location. Although finer resolutions may be achievable with increased magnification (i.e., smaller interrogation width and height), for a given aperture and illumination wavelength this comes at a cost of decreased depth of focus. The limited pulse energy of current-generation, kHz-rate DPSS lasers makes increasing one's illumination to compensate for this more challenging. The results of this study suggest that the somewhat course spatial resolution achievable with tomographic-PIV will be a significant limitation in many turbulent-flame interaction experiments.

Conclusion

The objective of this study was to test the feasibility of accomplishing kHz rate tomographic particle image velocimetry (tomographic-PIV) in a turbulent flame with currently available laser and camera technology. To this end, a four-camera tomographic-PIV system designed to replicate current-generation laser and imaging technology (albeit operated at 10 Hz) was applied to characterize the flow-field of a lifted turbulent jet flame fueled with methane. The interrogation volume was chosen to be $29 \times 28 \times 2.7$ mm in size, providing a reasonable compromise between field of view and spatial resolution. Reconstruction of the 3D particle distributions was accomplished using the multiplicative algebraic reconstruction technique.

In addition to demonstrating the feasibility of the measurement technique in turbulent combustion environment, a number of quality checks were applied to determine the signal-to-noise ratio, vector yield and achievable vector resolution. The results indicate that usable tomographic-PIV measurements in a turbulent flame are possible with laser pulse energies of 25mJ, which is well within the capability of current-generation kHz-rate diode-pumped solid state lasers; as expected, the quality of the measurement was higher with pulse energies of 40mJ. Furthermore, improvement in detection limits with the current generation of CMOS cameras is expected to reduce the required laser pulse energy and improve the measurement quality too. Equally important, it was found that index-of-refraction changes caused by the presence of a flame (either overlapped with the interrogation volume or between it and the cameras) do not significantly affect robustness or accuracy of the tomographic-PIV technique at the conditions for this study.

Acknowledgement

This work was supported by the Air Force Office of Scientific Research (AFOSR) and The European Office of Aerospace Research & Development (EOARD) through Grant FA8655-12-1-2092.

References

R.J. Adrian, *Ann. Rev. Fluid Mech.* **23**: 261-304 (1991)

I. Boxx, M. Stöhr, C. Carter, W. Meier. *Combust. Flame* **15**:8, 1510-1525 (2010)

B. Coriton, A.M. Steinberg, J.H. Frank. 8th U. S. National Combustion Meeting. Paper # 070DI0040.

G.E. Elsinga, F. Scarano, B. Wieneke, V.W. van Oudheusden, *Exp. Fluids* **41**, 933-947 (2006).

M. Gamba, N.T. Clemens, O.A. Ezekoye. *Meas. Sci. Technol.* **24**. 024003 (2013)

B. Ganapathisubramani, K. Lakshminarasimhan, N.T. Clemens. *J. Fluid Mech.* **598**:141-75 (2008).

S. Ghaemi, F. Scarano. *Meas. Sci. Technol.* **21**. 127002 (2010)

D. Han, L.K. Su, R.K. Menon, M.G. Mungal, Proc. of the Tenth International Symposium on Applications of Laser Techniques to Fluid Mechanics, Lisbon, Portugal. (2000).

B. Lecordier, C. Gobin, C. Lacour, A. Cessou, B. Tremblais, L. Thomas, L. David. 16th Int Symp on Applications of Laser Techniques to Fluid Mechanics. Lisbon, Portugal, 09-12 July, 2012.

H.G. Maas, A. Gruen, D. Papantoniou. *Exp. Fluids*, **15**:133-146 (1993)

L. Muniz, R.E. Martinez, M.G. Mungal, Proc. of the Eighth International Symposium on Applications of Laser Techniques to Fluid Mechanics, Lisbon, Portugal, 411-424. (1996)

P. Petersson, M. Gesnik, J. Olofsson, V. Jaunet, M. Aldén. Proceedings of the European Combustion Meeting 2013, Paper P3-15, June 25-28, 2013, Lund, Sweden. ISBN 978-91-637-2151-9.

S. Pfadler, F. Beyrau, A. Leipertz. *Opt. Express*. **15**:444. 15:23 (2007).

S. Pfadler, F. Dinkelacker, F. Beyrau, A. Leipertz, *Combust. Flame* **156**, 1552–1564 (2009).

S. Pfadler, F. Beyrau, F. Dinkelacker, A. Leipertz, *Exp. Fluids* **49**, 839–851. (2010)

F. Scarano, *Meas. Sci. Technol.* **24**. 012001 (2013)

A. Steinberg, J. Driscoll, S. Ceccio. *Exp. Fluids* **47**:527-47 (2009)

J. Westerweel, F. Scarano. *Exp. Fluids*, **39**:1096–1100 (2005)

B. Wieneke. *Exp Fluids*. **45**:549–556 (2008)

Figures

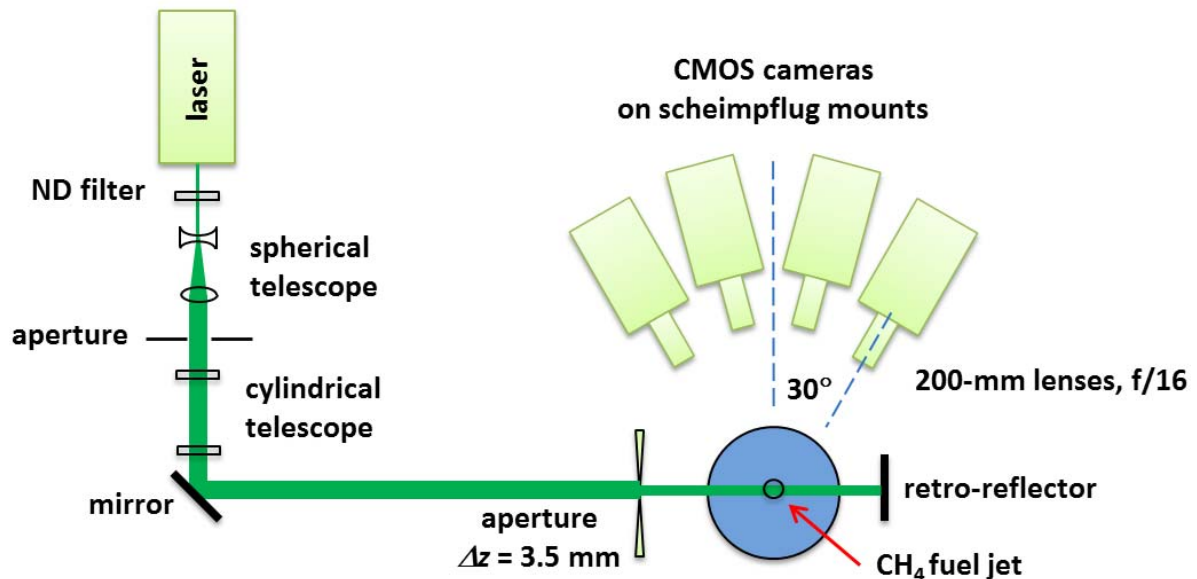


Figure 1 – Experimental Setup.

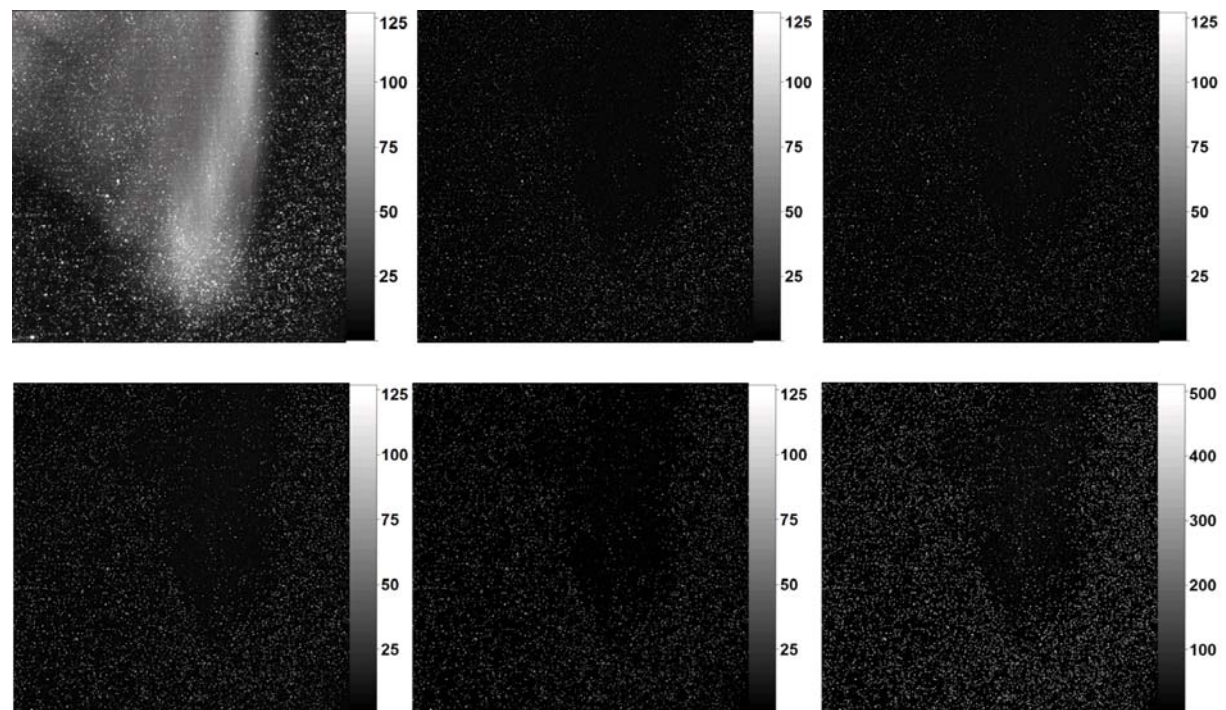


Figure 2. Image pre-processing steps. a) Raw particle image, b) Subtract sliding minimum, c) Local averaging, d) Smoothen/Smoothing, e) subtract constant background, f) multiply by constant (note expanded color bar).

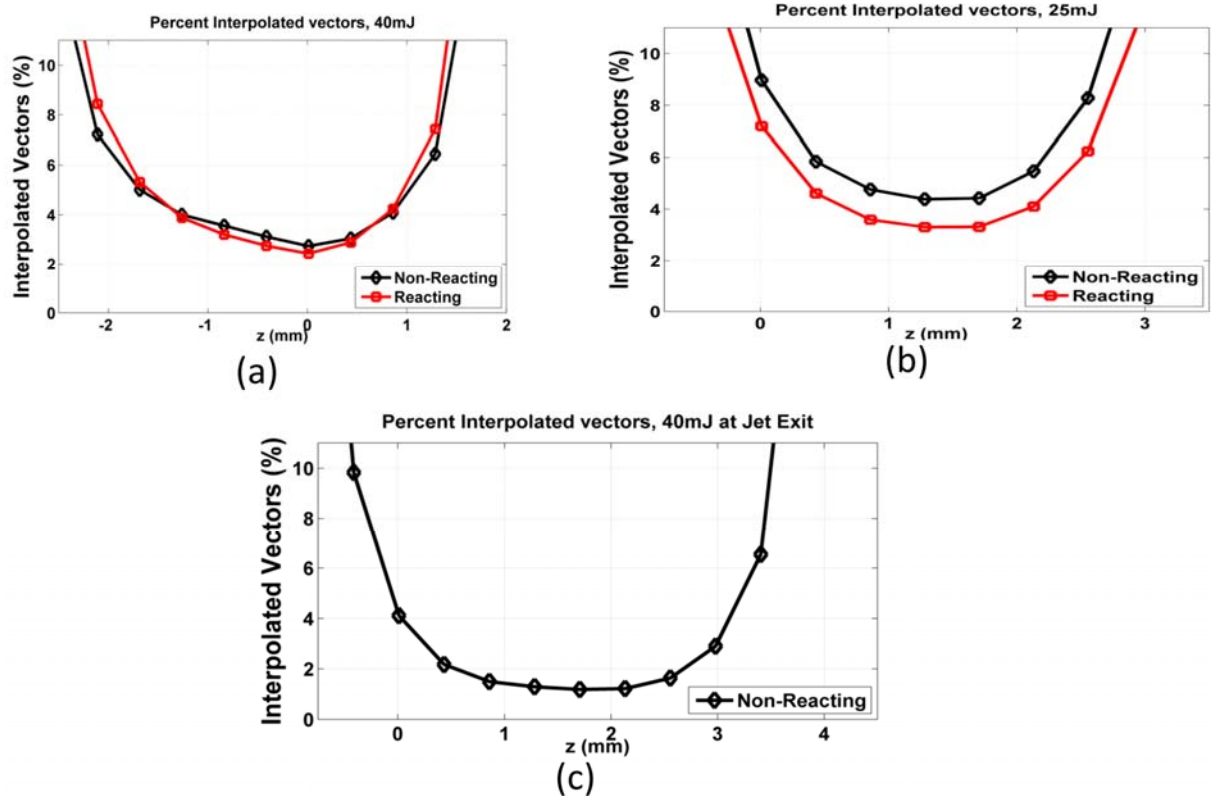


Figure 3. Percentage of vectors removed and replaced in validation. a) Downstream location, 40mJ/pulse. b) Downstream location 25mJ/pulse, c) Jet-exit location (non-reacting).

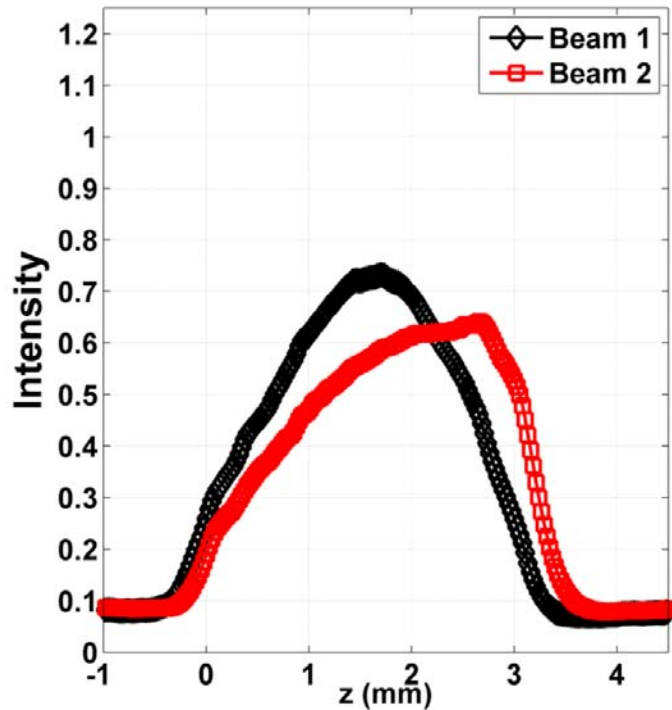


Figure 4. Laser illumination in the z -direction at jet-exit location.

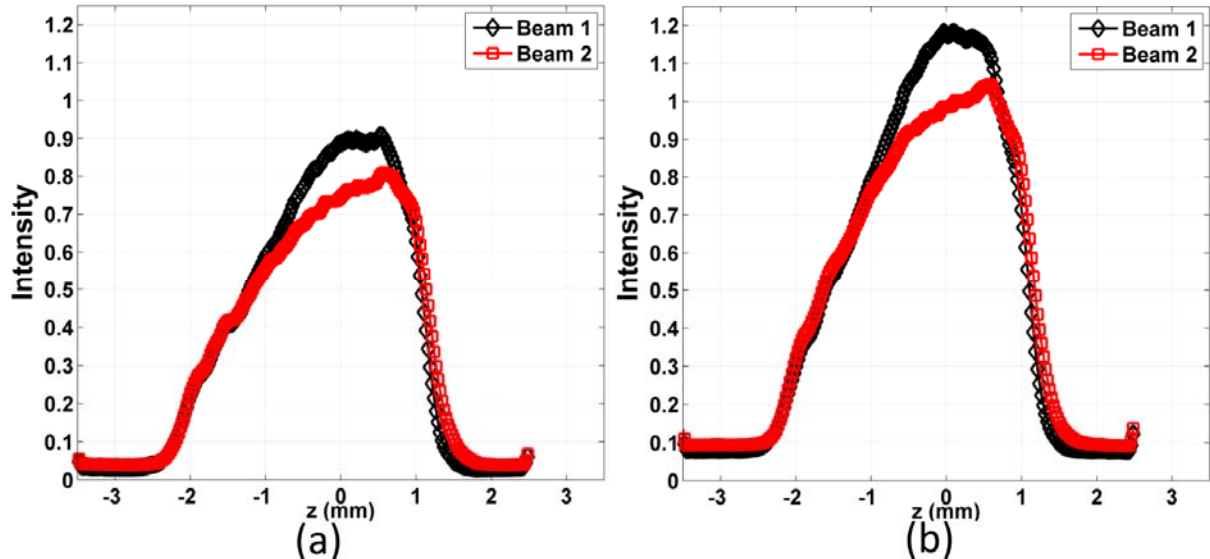


Figure 5. Laser illumination in the z -direction for cases with 40mJ illumination, with retro-reflection. a) Non-reacting jet, b) Lifted jet-flame.

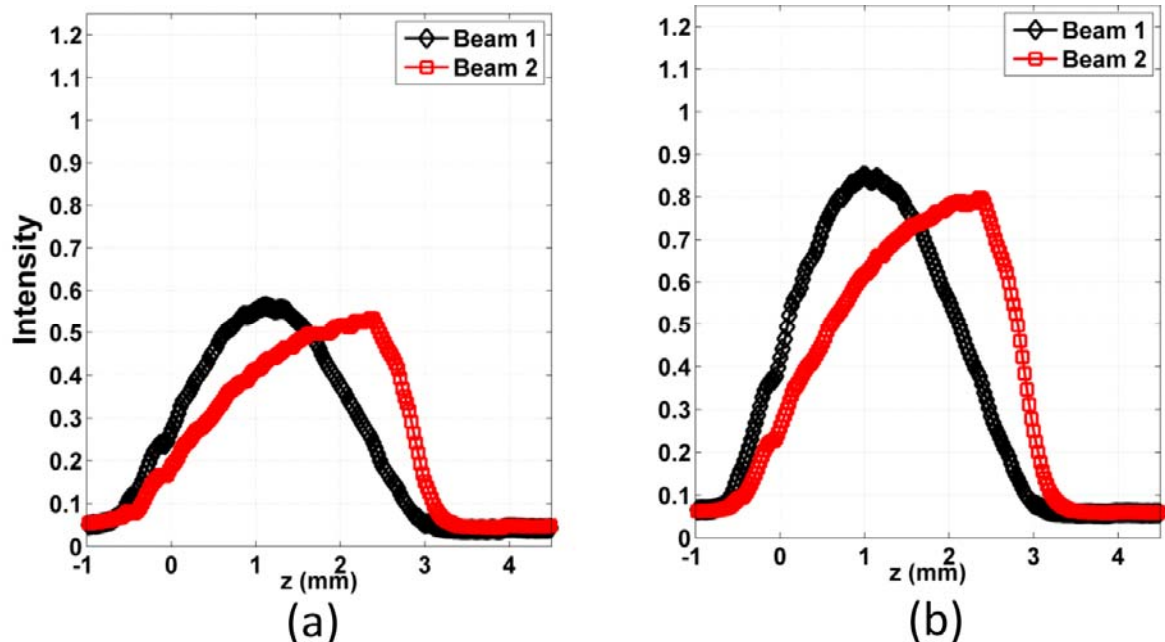


Figure 6. Laser illumination in the z -direction for cases with 25mJ illumination, with retro-reflection. a) Non-reacting jet, b) Lifted jet-flame.

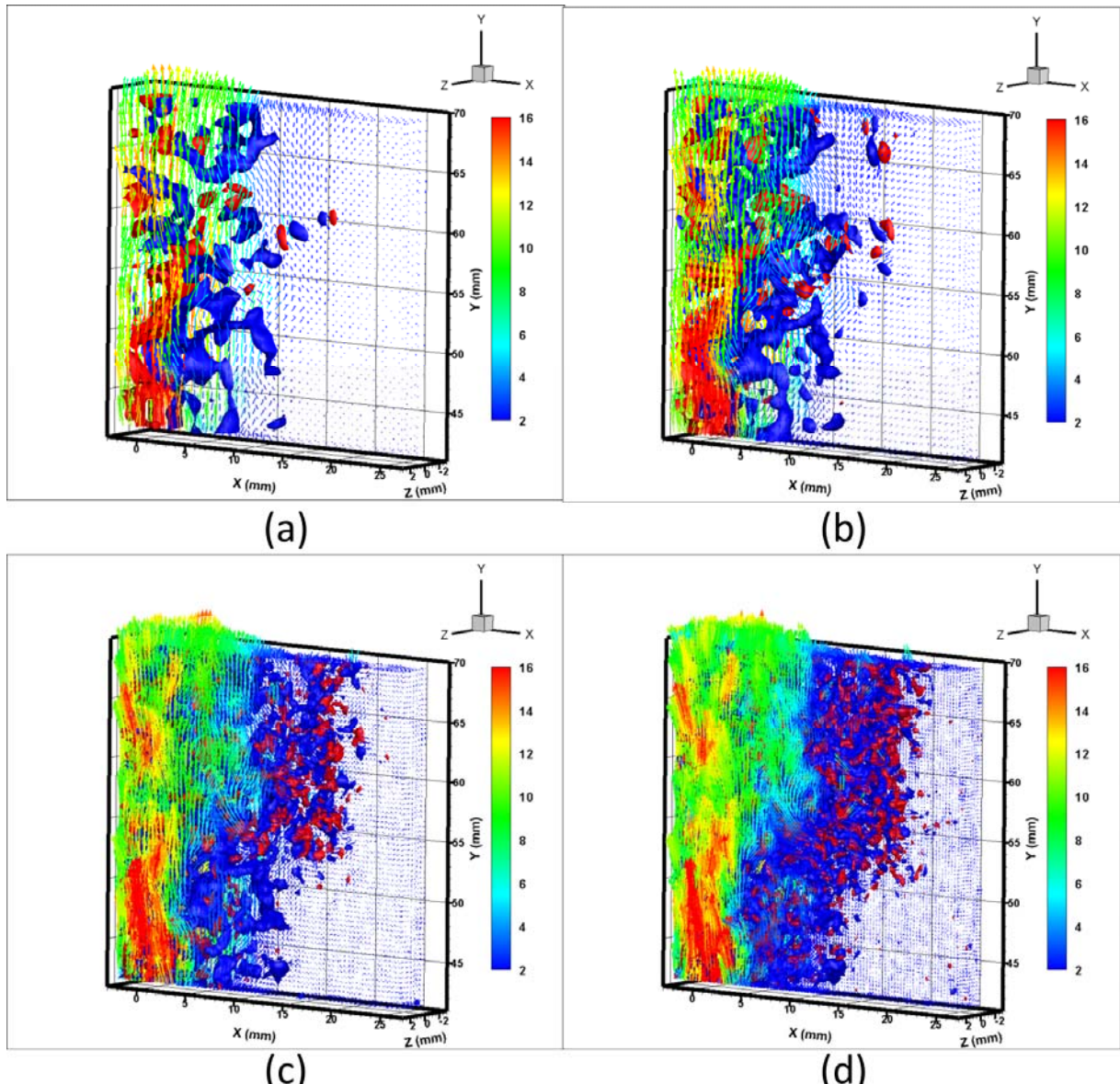


Figure 7. Vector resolution vs. Noise in a lifted jet flame. a) $64 \times 64 \times 64$, b) $48 \times 48 \times 48$, c) $32 \times 32 \times 32$, d) $24 \times 24 \times 24$ voxels

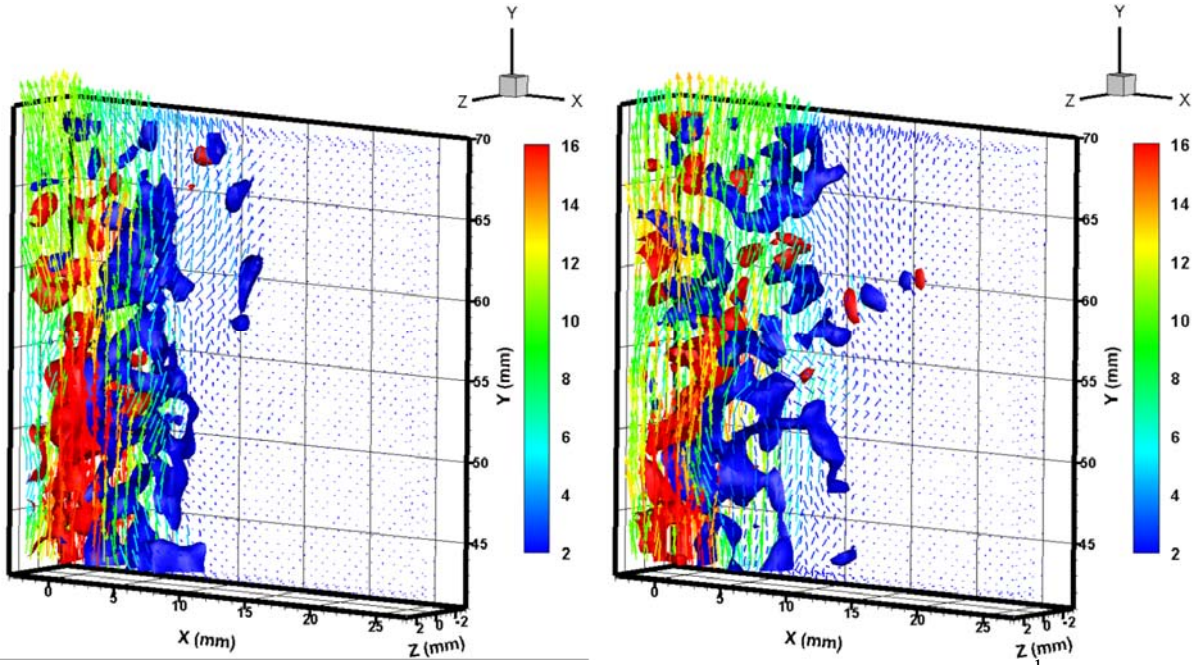


Figure 8. Instantaneous velocity field and vorticity isocontours ($\pm 2500\text{s}^{-1}$) for 40mJ illumination and laser retro-reflection. a) Non-reacting jet and b) Lifted jet-flame

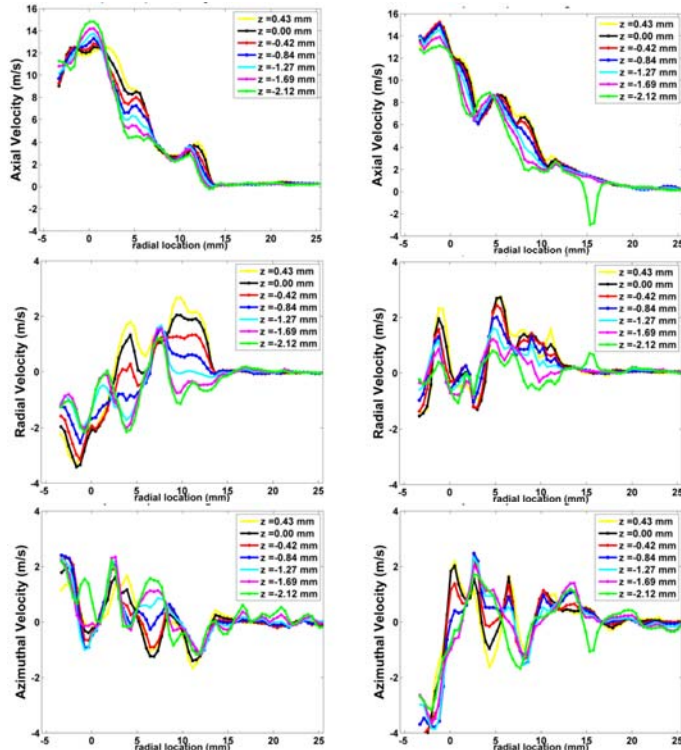


Figure 9. Single-shot profiles of each velocity component. Measured 60mm downstream of jet-exit with 40mJ illumination and laser retro-reflection. Left – Nonreacting jet. Right – Lifted Jet flame.

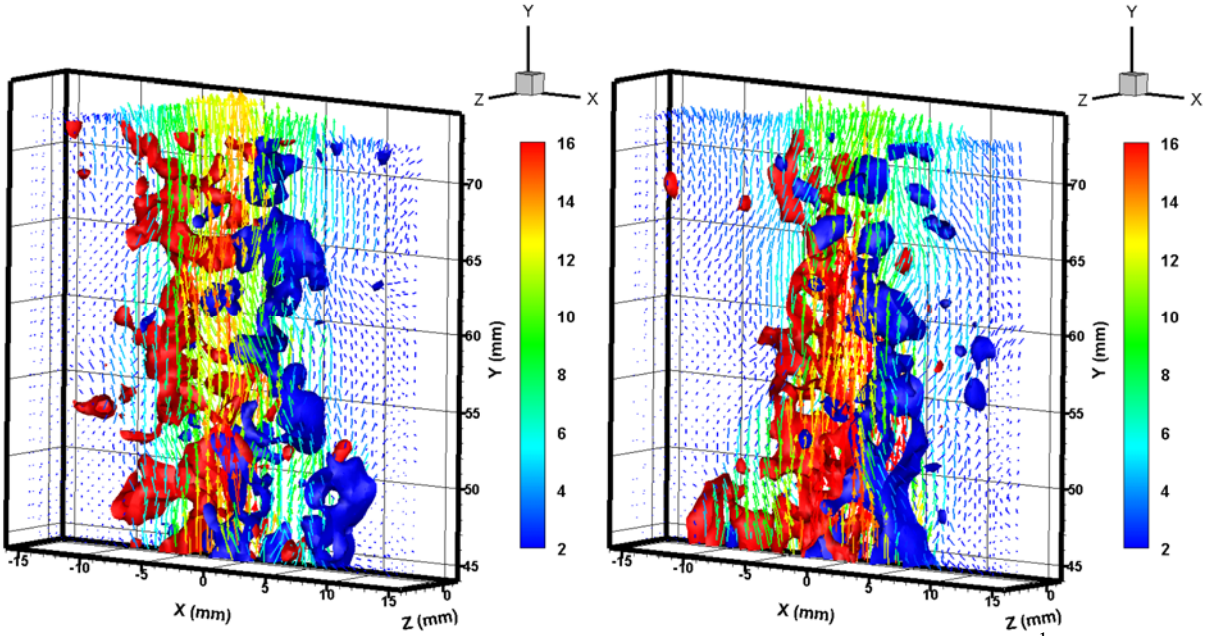


Figure 10. Instantaneous velocity field and vorticity isocontours ($\pm 2500 \text{s}^{-1}$) for 25mJ illumination and laser retro-reflection. a) Non-reacting jet and b) Lifted jet-flame.

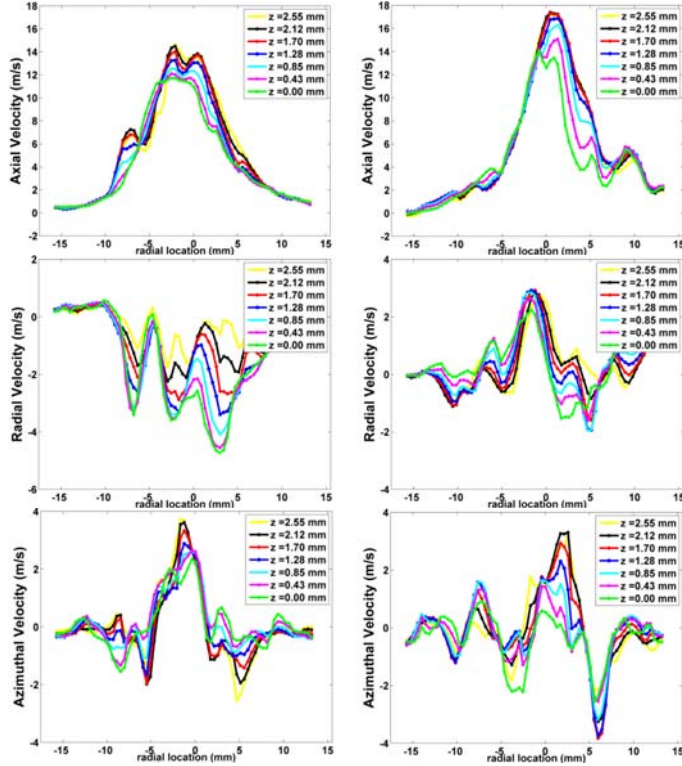


Figure 11. Single-shot profiles of each velocity component. Measured 60mm downstream of jet-exit with 25mJ illumination and laser retro-reflection. Left – Non-reacting jet. Right – Lifted Jet flame.

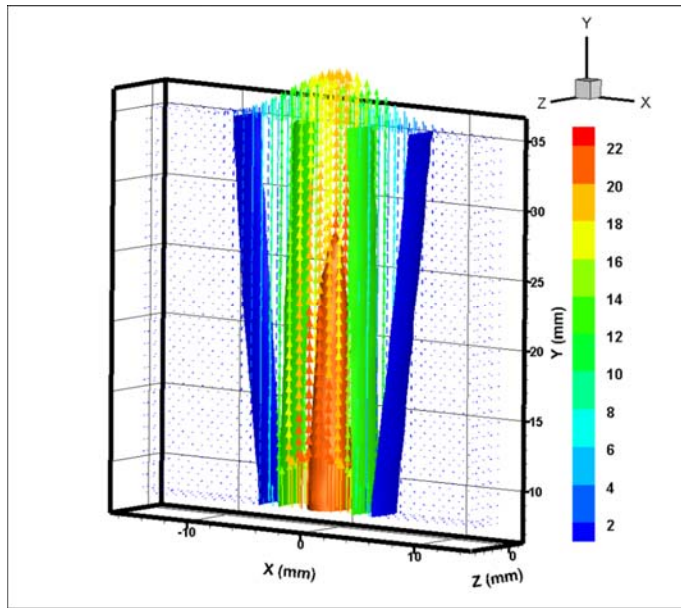


Figure 12. Mean axial velocity, at $64 \times 64 \times 64$ voxels, 40mJ illumination.

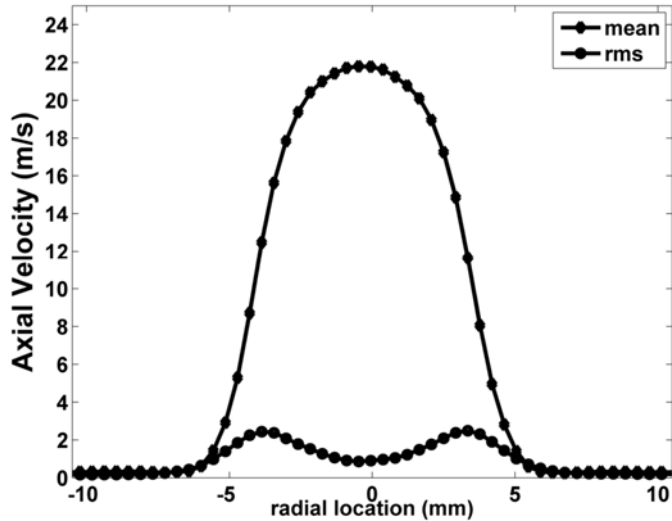


Figure 13. Mean and rms (axial) velocity profiles 8mm downstream of the jet-exit.

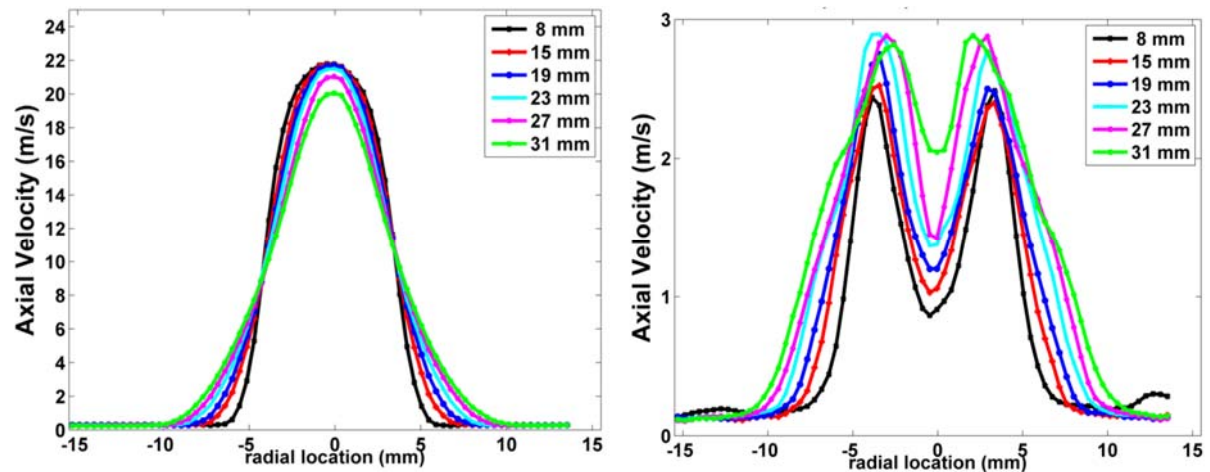


Figure 14. a) Mean axial velocity b) Fluctuating axial velocity in jet near-field

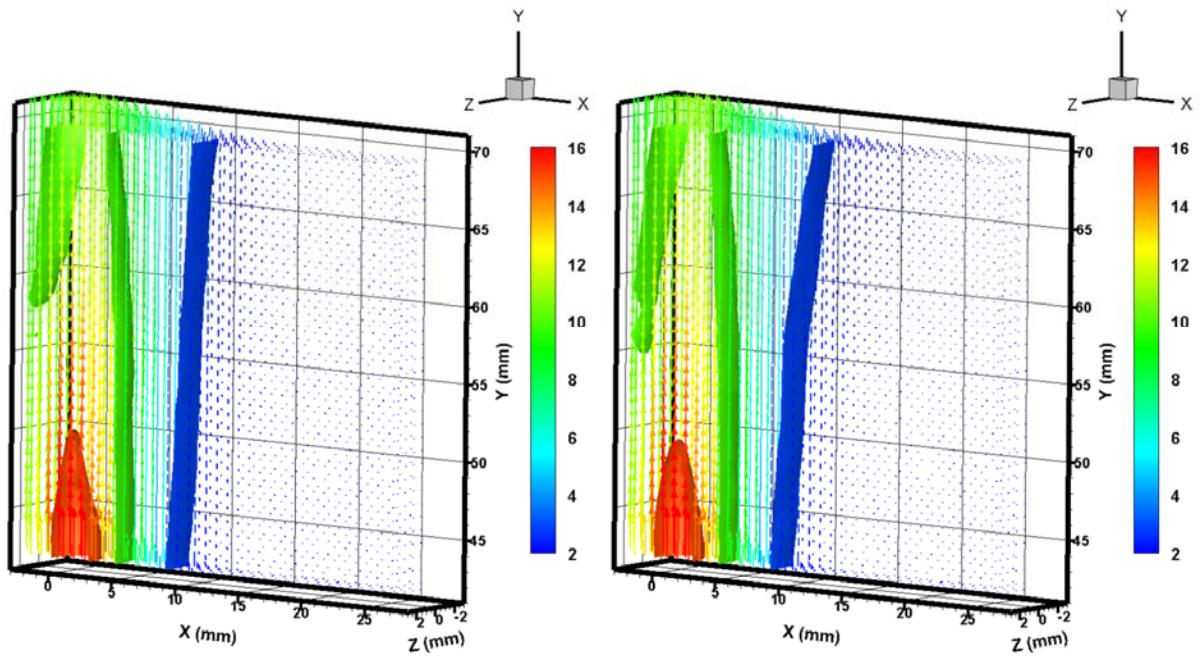


Figure 15. Mean axial velocity, at $64 \times 64 \times 64$ voxels, 40mJ illumination. a) Non-reacting jet. b) Lifted jet-flame.

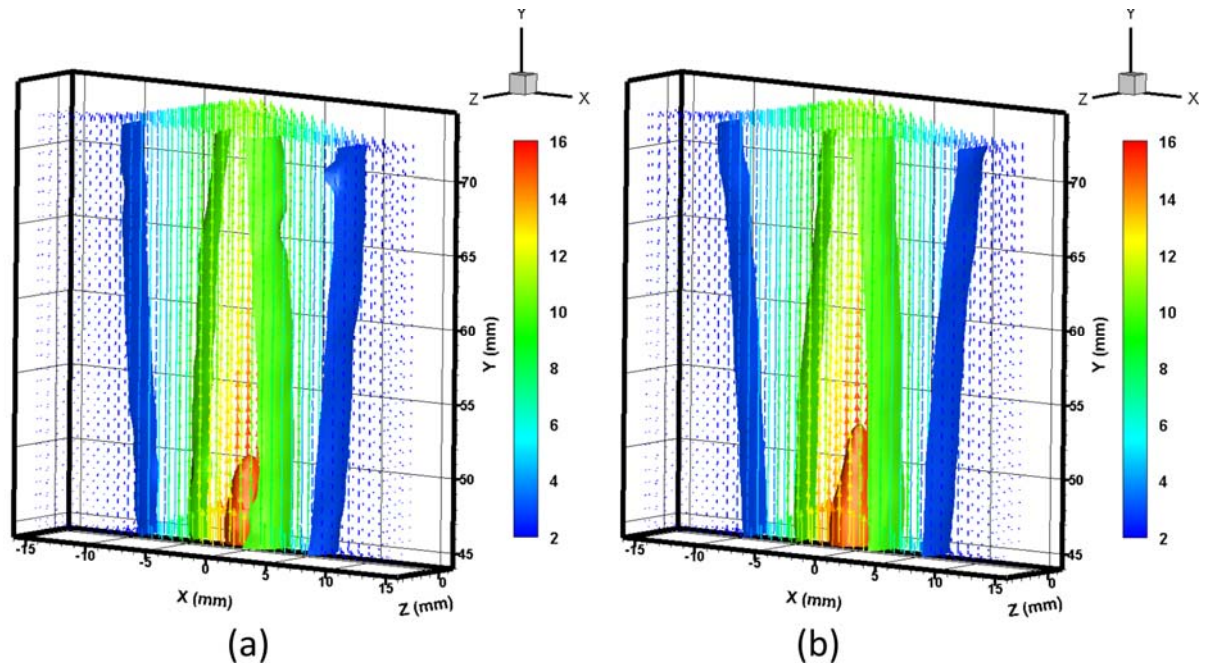


Figure 16. Mean axial velocity, at $64 \times 64 \times 64$ voxels, 25mJ illumination. a) Non-reacting jet. b) Lifted jet-flame.

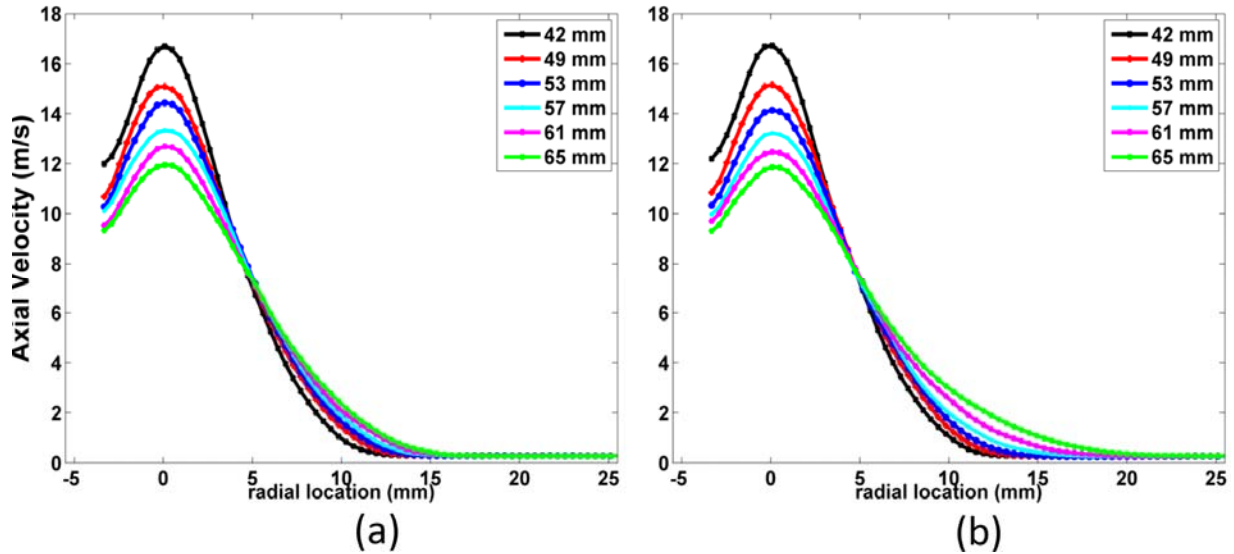


Figure 17. Mean axial velocity measured with 40mJ, with retro-reflection. a) Non-reacting jet and b) Lifted jet-flame.

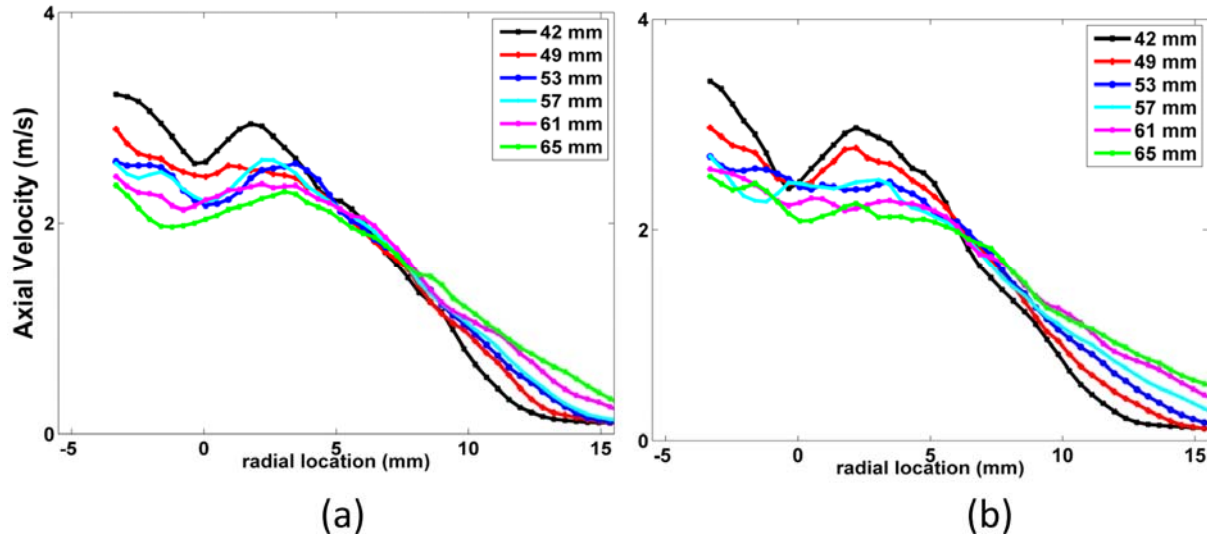


Figure 18. RMS axial velocity measured with 40mJ, with retro-reflection. a) Non-reacting jet and b) Lifted jet-flame.

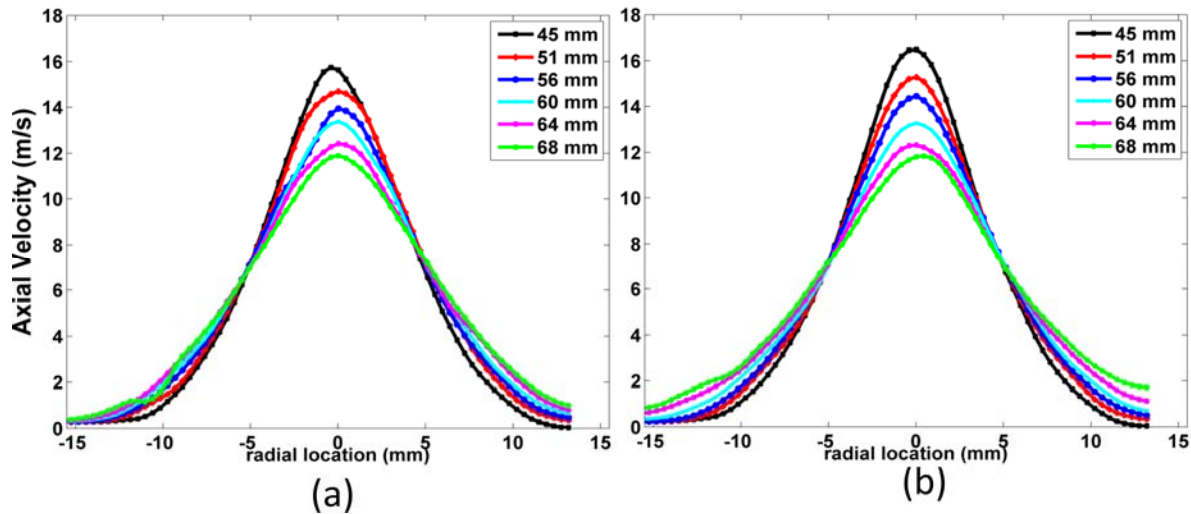


Figure 19. Mean axial velocity measured with 25mJ, with retro-reflection. a) Non-reacting jet and b) Lifted jet-flame.

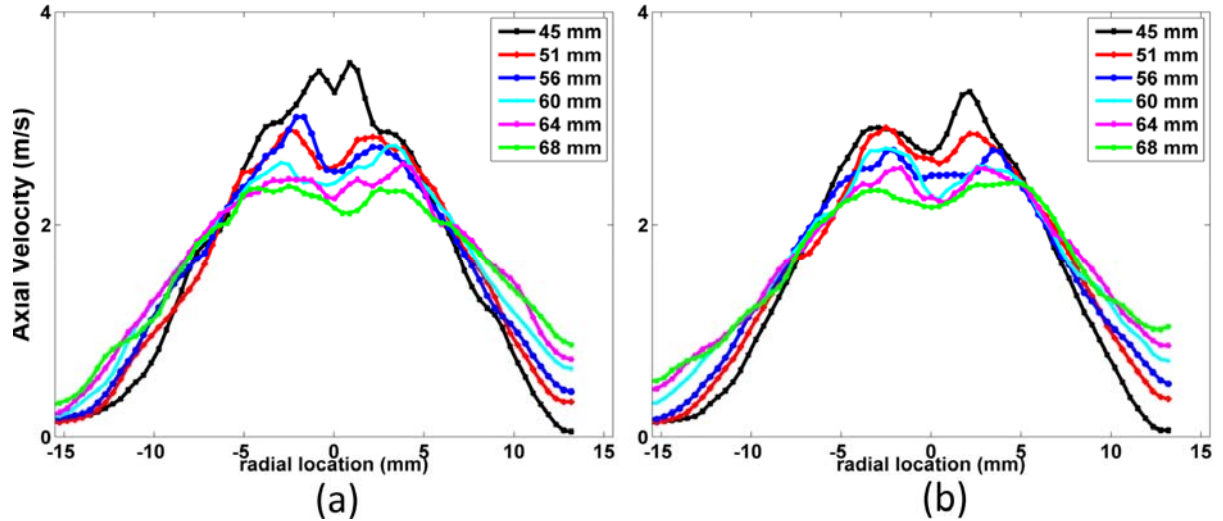


Figure 20. RMS axial velocity measured with 25mJ, with retro-reflection. a) Non-reacting jet and b) Lifted jet-flame.

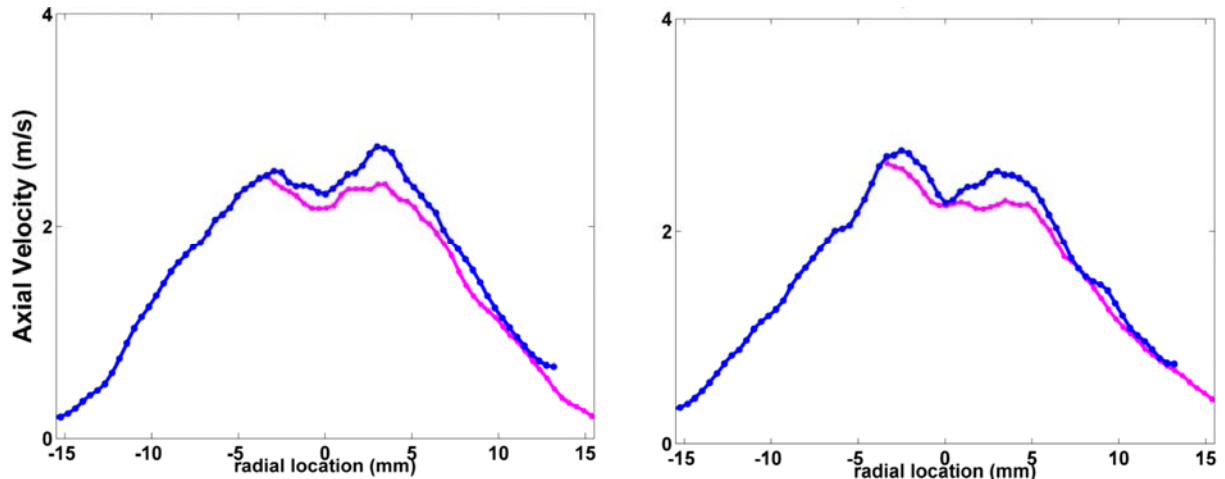


Figure 21. RMS axial velocity profiles, measured 60mm from jet-exit with the purple and blue lines corresponding to 40 and 25mJ illumination, respectively. a) Non-reacting jet and b) Lifted jet-flame.